

Radio-frequency charge detection on graphene electron-hole double quantum dots

K. Hecker,^{1,2,*} S. Möller,^{1,2,*} H. Dulisch,^{1,2} Ş. Duman,³ L. Stecher,¹ L. Valerius,^{1,†} T. Deußen,¹ S. Ravuri,¹ K. Watanabe,⁴ T. Taniguchi,⁵ F. Libisch,³ C. Volk,^{1,2} and C. Stampfer^{1,2,‡}

¹*JARA-FIT and 2nd Institute of Physics, RWTH Aachen University, 52074 Aachen, Germany, EU*

²*Peter Grünberg Institute (PGI-9), Forschungszentrum Jülich, 52425 Jülich, Germany, EU*

³*Institute for Theoretical Physics, TU Wien, 1040 Vienna, Austria, EU*

⁴*Research Center for Electronic and Optical Materials,*

National Institute for Materials Science, 1-1 Namiki, Tsukuba 305-0044, Japan

⁵*Research Center for Materials Nanoarchitectonics,*

National Institute for Materials Science, 1-1 Namiki, Tsukuba 305-0044, Japan

(Dated: September 16, 2025)

High-fidelity detection of charge transitions in quantum dots (QDs) is a key ingredient in solid state quantum computation. We demonstrate high-bandwidth radio-frequency charge detection in bilayer graphene quantum dots (QDs) using a capacitively coupled quantum point contact (QPC). The device design suppresses screening effects and enables sensitive QPC-based charge readout. The QPC is arranged to maximize the readout contrast between two neighboring, coupled electron and hole QDs. We apply the readout scheme to a single-particle electron-hole double QD and demonstrate time-resolved detection of charge states as well as magnetic field dependent tunneling rates. This promises a high-fidelity readout scheme for individual spin and valley states, which is important for the operation of spin, valley or spin-valley qubits in bilayer graphene.

A fast and state-selective readout method is a prerequisite for operating semiconductor quantum dots (QDs) as hosts for qubits [1]. It is a well-established technique to use capacitively coupled quantum point contacts (QPCs) or single-electron transistors to read out charge transitions in semiconductor QDs [2, 3]. Typically, the conductance of the charge detector is either measured directly by transport [4, 5] or indirectly via the reflectance of an impedance matched LC resonant circuit connected to the charge detector [6, 7] to reach a higher bandwidth [8]. This technique enables time-resolved single-shot detection of charge and spin states in current semiconductor devices [7, 9–16]. Graphene and bilayer graphene (BLG), with their naturally low hyperfine interaction and low spin-orbit coupling, offer a promising new platform for spin- and valley-based qubits [17–20]. BLG is of particular interest thanks to its gate voltage tunable band gap [21] that allows the formation of QPCs and QDs [22–25]. So far, the energy spectra of single- [26, 27] and two-particle BLG QD states [28] have been investigated and single-particle spin and valley relaxation times have been studied by standard DC transport techniques [29, 30]. Blockade mechanisms of spin and valley states have been demonstrated in BLG double QDs (DQDs) [31–33] as well as a particle-hole symmetry protected spin-valley blockade [34]. In addition, charge sensing has been successfully implemented in BLG QD devices, both by transport measurements of a capacitively coupled QD [35] and by dispersive readout techniques [36, 37]. This allowed for time-resolved detection of charge carriers in

QDs [38, 39] and DQDs [40] in the Hz to low kHz regime. Nevertheless, to study real-time dynamics of QDs, charge detection with a high single-shot bandwidth is crucial.

Here, we present radio-frequency (RF) reflectometry detection of charge states in an electron-hole DQD, both via time-averaged and time-resolved measurements. The RF reflectometry technique allows to reach a bandwidth of up to several MHz. The device has been tailored towards maximum readout contrast between the electron and hole QDs by an in-line arrangement of the QPC with the QDs. We find that the in-plane capacitive coupling can be improved by reducing the charge carrier density between the QDs and the QPC charge detector. We identify the effects of screening and the lateral distance between the QDs and the detector on its sensitivity by comparison with a self-consistent Schrödinger-Poisson solver. Finally, we perform charge detection in the time domain at the interdot transition of a weakly coupled single-particle electron-hole DQD. Thereby, we study the magnetic field dependence of single electron-hole tunneling rates. Time-resolved charge-detection of single-particle electron-hole DQDs marks an important step towards the readout of spin and valley qubits in BLG [20] or wide band terahertz photon detection [41].

The device consists of a heterostructure of BLG encapsulated between two crystals of hexagonal boron nitride (hBN), each ≈ 50 nm thick, placed on a graphitic back gate (BG). Split gates (SGs, see Fig. 1a) are used to form conducting channels. In the wide channel (highlighted in blue in Fig. 1a), a QPC beneath the finger gate G0 (orange) acts as a capacitively coupled charge detector. This channel forms a T-junction with the narrow channel beneath the other finger gates (FGs), where the QDs will be localized. This gate architecture is tailored to enhance the capacitive coupling between detector and QDs, in particular to optimize the sensitivity to interdot charge

* These two authors contributed equally.

† Present address: Department of Physics, Humboldt Universität zu Berlin, 12489 Berlin, Germany

‡ stampfer@physik.rwth-aachen.de

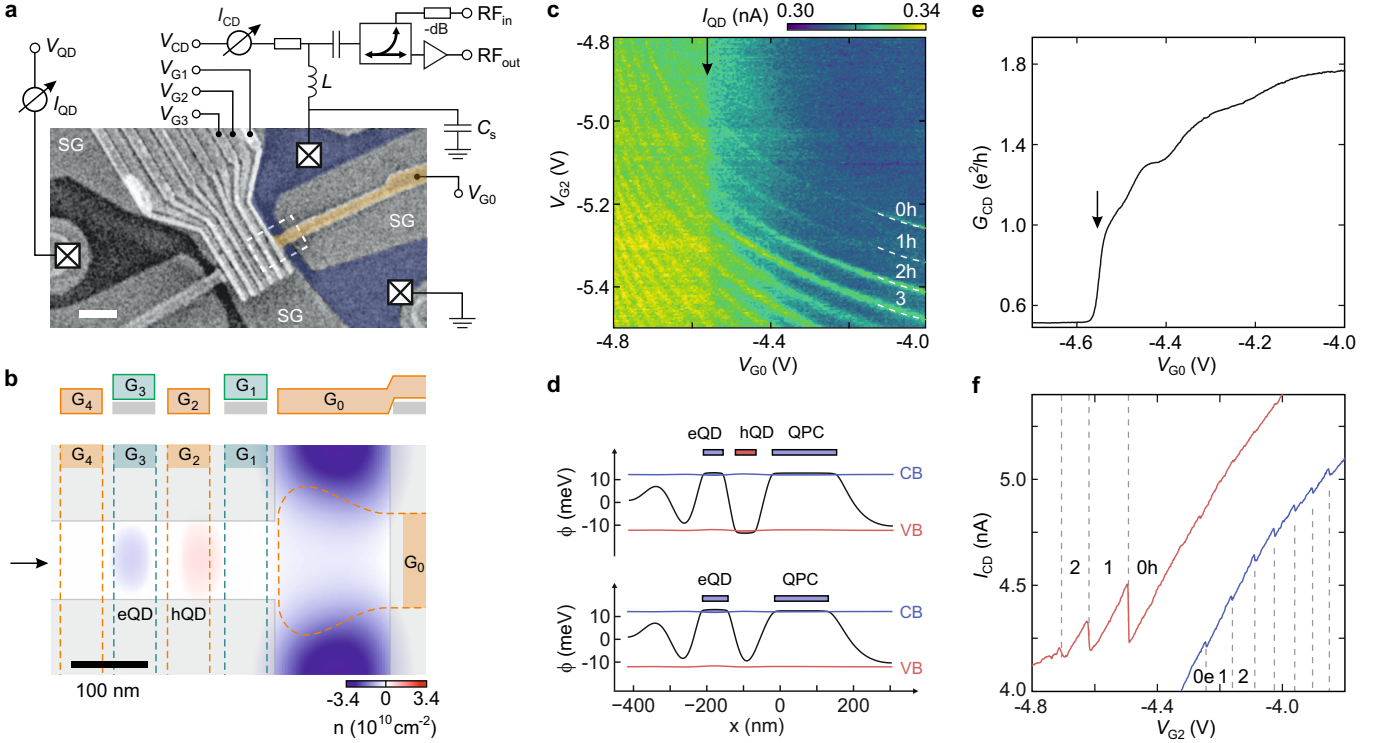


FIG. 1. (a) False-colored scanning electron microscopy image of the BLG QD device. Scale bar is 500 nm. Split gates (SGs) define conducting channels; finger gates G1–G3 control the potential along the narrow channel, defining and controlling QDs and gate G0 (orange) defines a QPC in the wide channel (blue) acting as charge detector. Via three ohmic contacts (\boxtimes) bias voltages can be applied and current through the device can be measured. One of the contacts is additionally connected to an inductor, $L = 3.3 \mu\text{H}$, forming an LC resonant circuit together with the stray capacitance of the bond wires, $C_s \approx 0.6 \text{ pF}$, matching the impedance of the QPC to the 50Ω RF line. For reflectometry measurements, an RF signal (RF_{in}) is applied to the resonant circuit via cryogenic attenuators (-36 dB) and a directional coupler (-20 dB). The reflected signal is amplified (35 dB , Cosmic Microwave CITLF3) at 4 K , followed by additional 28 dB at room temperature. A lock-in amplifier (Zurich Instruments UHFLI 600 MHz) is used for signal generation and homodyne detection. (b) Schematic of the gate structure together with the calculated charge carrier density n induced in the BLG (scale bar is 100 nm). For the calculation the gate voltages were chosen as $V_{\text{G1}} = -4.44 \text{ V}$, $V_{\text{G2}} = -4.795 \text{ V}$, $V_{\text{G3}} = -3.52 \text{ V}$, $V_{\text{G4}} = -4.54 \text{ V}$, $V_{\text{G0}} = -4.17 \text{ V}$, $V_{\text{SG}} = -3.88 \text{ V}$, $V_{\text{BG}} = 4 \text{ V}$. (c) Current I_{QD} as a function of the gate voltages V_{G0} and V_{G2} with $V_{\text{CD}} = 250 \mu\text{V}$, $V_{\text{QD}} = 0$. Coulomb resonances of a hole QD formed in the narrow channel close to the T-junction appear. The vertical feature (see arrow) is caused by the formation of a QPC in the wide channel. (d) Potential profiles along the narrow channel (black lines) in between bulk conduction (CB) and valence band (VB) for two different gate voltage configurations defining an electron-hole DQD (upper panel, corresponding to b)) and an electron QD (lower panel). (e) Conductance G_{CD} of the charge detector operated in the QPC regime ($V_{\text{CD}} = 80 \mu\text{V}$). The arrow indicates the operating point set in the following experiments. (f) Jumps in I_{CD} as a function of V_{G2} (see labels and dashed lines) show the formation of QDs (see text) in the few hole ($V_{\text{G4}} = -4.3 \text{ V}$, red) and few electron ($V_{\text{G4}} = -5.35 \text{ V}$, blue, offset by -0.5 nA for clarity) regimes.

transitions, following designs of other semiconductor QD devices [13]. For details on device design and fabrication, we refer to the Supplementary Material and to Ref. [25].

Fig. 1b shows a schematic of the top gates at the T-junction (dashed box in Fig. 1a) together with the simulated charge carrier density in the BLG for an exemplary set of gate voltages to illustrate how the device is operated. Here, electron and hole QDs are formed below the FGs, while a QPC is formed below gate G0 at the T-junction. The simulation is based on a self-consistent Schrödinger-Poisson solver, where a full 3D model of our device was implemented by an adaptive finite element grid with the NGSolve software package [42] (see Supple-

mentary Material).

In the following, the channels between the split gates are set to an n-type polarity by applying a positive voltage to the BG. By applying negative voltages to V_{G0} and V_{G2} forms an n-type QPC in the wide channel and a hole QD in the narrow channel in agreement with the carrier density calculation presented in Fig. 1b. We investigate this QPC-QD system by measuring the current through the narrow channel, I_{QD} , as a function of V_{G0} and V_{G2} , depicted in Fig. 1c. Coulomb resonances indicate the formation of a hole QD, which occupation can be controlled by V_{G2} (occupation 0h, 1h, etc.). With decreasing voltage V_{G0} , the hole QD is dragged towards the charge de-

tector, as shown by the curvature of the Coulomb peaks. We measure the conductance $G_{CD} = I_{CD}/V_{CD}$ of the wide channel as a function of V_{G0} , which is depicted in Fig. 1e, where quantized steps indicate the formation of a QPC. The pinch off of the QPC conductance leads to the change in background current in Fig. 1c (see arrow). The residual conductance below the pinch off originates from a parallel conductive channel which is not controlled by the gate voltage V_{G0} , limiting the maximum resistance to 50 k Ω . To optimize the sensitivity of the charge detector, the QPC is tuned to its steepest flank, highlighted by the arrow in Fig. 1e, where slight changes in the capacitive environment of the QPC translate into strong changes of its resistance. To reduce screening of the capacitive coupling between the charge detector and the QDs, G1 is used to deplete the charge carrier density in between the QPC and the right most QD (see Fig. 1b). This results in a low tunnel coupling, where transport through the QDs can no longer be measured directly. However, by measuring the current I_{CD} , the charge occupation of the QDs can be measured indirectly. Fig. 1f shows I_{CD} as a function of V_{G2} . By decreasing V_{G2} , a hole QD forms under FG G2 (compare with Fig. 1b). The number of holes occupying the QD under G2 increases, starting from an empty hole QD (red trace in Fig. 1f). Each charge transition causes a sharp jump in I_{CD} . When applying a more negative voltage of $V_{G4} = -5.35$ V, a barrier is formed in the channel, which leads to an electron QD emerging below G3 (compare with Fig. 1b). With decreasing V_{G2} , this electron QD is emptied, which can be seen in jumps in I_{CD} due to charging events for further increasing V_{G2} (blue trace in Fig. 1f). In this case, the step height of the charge detector response is less pronounced due to the weaker capacitive coupling caused by the larger distance between the electron QD and the QPC charge detector. The simulations of the corresponding band edge profiles along the center of the narrow channel are shown in Fig. 1d. Here, the black curve is the calculated electrostatic potential ϕ varying in between the bulk conduction and valence band edges. The charge carrier occupations of the individual QDs can be changed by varying the gate voltages, allowing to form e.g. a single electron QD or an electron-hole DQD.

To improve on the bandwidth and the signal-to-noise ratio (SNR) of the detection signal, we use a radio frequency reflectometry technique. Therefore, we excite the resonant circuit and measure the reflected signal in a homodyne demodulation scheme. Fig. 2a shows the magnitude R_{demod} of the demodulated signal as a function of the excitation frequency f for voltages applied to the detector gate between $V_{G0} = -4.6$ V and -4.5 V. The total resistance of the charge detector, including the channel resistance and contact resistances, does not reach the matching condition of $R_{CD} = 100$ k Ω , since it is limited to 50 k Ω (c.f. Fig. 1e). However, a change of 1.5 dBm can still be observed at resonance ($f_{\text{res}} = 115$ MHz).

To quantify the performance of the charge detector using the RF reflectometry technique, we focus on its

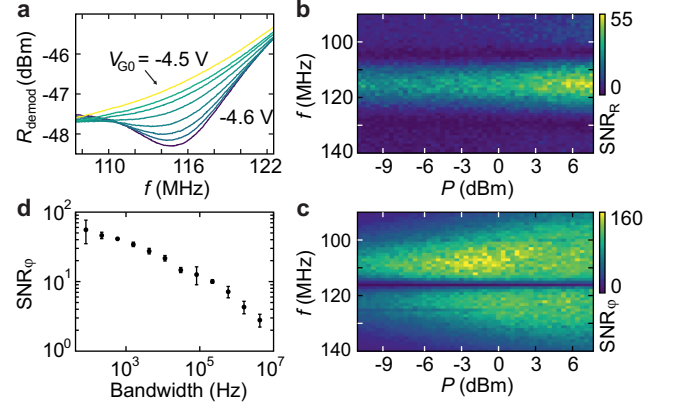


FIG. 2. (a) Magnitude of the RF signal as a function of the RF carrier frequency f for different voltages V_{G0} applied to the detector gate (excitation power $P = -10$ dBm). At the resonance frequency f_{res} of the tank circuit, the reflected signal is minimized. (b) Signal-to-noise ratio (SNR) of the magnitude R_{demod} of the RF signal reflected off the charge detector, measured as a function of f and P . The SNR is determined as the ratio of the step height of the first charge transition and the RMS of the noise. (c) SNR of the phase φ of the RF signal. (d) SNR of the phase response as a function of the measurement bandwidth ($P = -11$ dBm).

response to the first charge carrier being loaded to the hole QD. We investigate the SNR, which is defined by $\text{SNR}_R = \delta R_{\text{step}}/\langle R \rangle$ and $\text{SNR}_\varphi = \delta \varphi_{\text{step}}/\langle \varphi \rangle$, where δR_{step} and $\delta \varphi_{\text{step}}$ are the height of the step induced by the addition of a single charge in the demodulated amplitude (R) or phase (φ). $\langle R \rangle$ and $\langle \varphi \rangle$ are the standard deviation of the signal. Fig. 2b shows SNR_R as a function of the excitation frequency f and power P . As expected, SNR_R reaches its maximum at resonance and increases with P . The SNR of the phase, SNR_φ , shows an off-resonance maximum of 160 for P in the range of -3 to 0 dBm (see Fig. 2c). This is three times larger than the maximum SNR_R achieved at a larger excitation, $P = 6$ dBm. We attribute the reduced SNR_φ at $P > 0$ dBm to power broadening of the phase response. SNR_φ shows the expected scaling with the measurement bandwidth (see Fig. 2d), indicating an SNR above unity up to a bandwidth above 10 MHz. However, the current setup is limited by the sampling rate of the used RF lock-in amplifier to 7 MHz.

In addition to the power and frequency of the applied RF carrier, the sensitivity of the charge detector is also influenced by the lateral distance of the QDs and the QPC as well as screening effects due to a finite charge carrier density in between them. To investigate these effects, we measure the response of the charge detector on the electron and hole QD charge states using RF reflectometry, while varying the voltage V_{G1} applied to the gate in between the QPC and QDs. The charge stability diagram in Fig. 3a shows the derivative of the phase of the reflected signal, $d\varphi/dV_{G2}$ as a function of V_{G1} and V_{G2} . To keep the charge detector at its operating point,

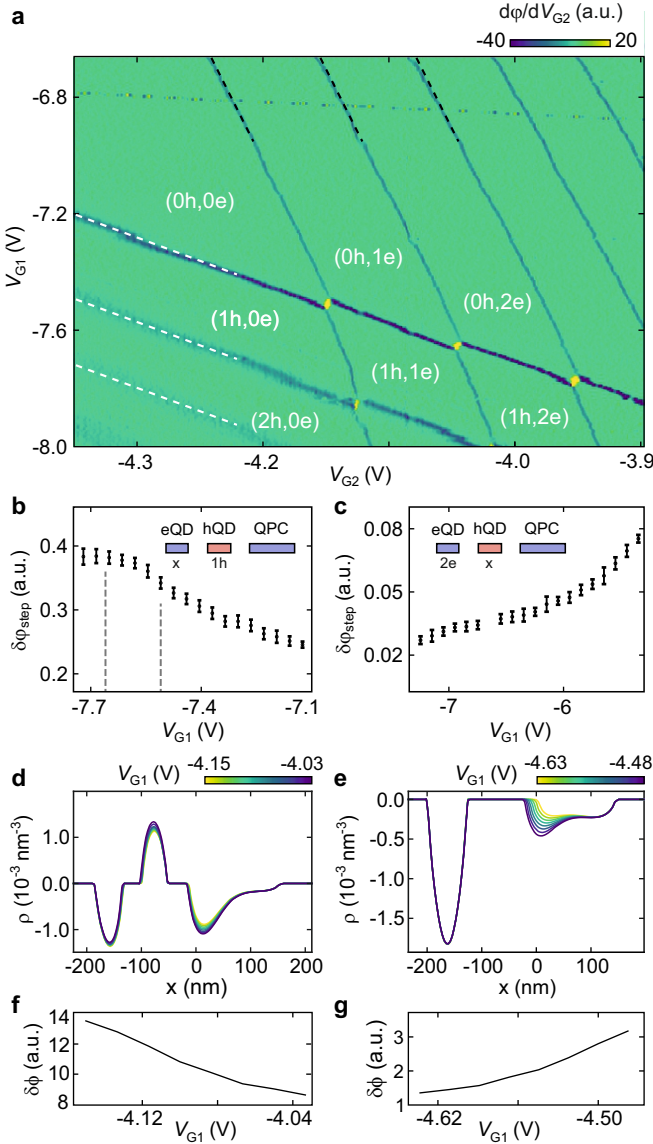


FIG. 3. (a) Charge stability diagram of the differential phase $d\phi/dV_{G2}$ of the reflected RF signal as a function of the gate voltages V_{G1} and V_{G2} . A hole (electron) QD is defined under gate G1 (G2). The charge carrier occupation of electron (e) and hole (h) QD (see labels) can be tuned down to (0h,0e). (b-c) Step height $\delta\phi_{\text{step}}$ of the charge detector response at the (b) 0h-1h, (c) 1e-2e charge transition (dashed lines in (a)) as a function of V_{G1} . Charge transitions of the electron QD occur at the gate voltages indicated by dashed lines. The inset depicts the corresponding charge configuration. (d-e) Line cut of the charge carrier density ρ along $y = 0$ in Fig. 1b calculated for different V_{G1} . The gate voltages $V_{G2} - V_{G4}$ have been chosen such that (d) the hole QD is occupied by roughly 1 hole and (e) the electron QD contains two electrons. (f-g) Average calculated potential difference $\delta\phi$ at the QPC due to a change in occupation of (f) the hole QD (g) the electron QD as a function of V_{G1} for the configurations shown in the insets of (b) and (c), respectively.

we correct for electrostatic cross-talk from gate G1 by

varying V_{G0} according to $V_{G0} = -4.737 \text{ V} - 0.0193 \cdot V_{G1}$.

The (0h,0e) region in the upper left of the charge stability diagram (Fig. 3a) corresponds to both QDs being empty. Sweeping V_{G1} to more negative values loads holes into the QD between G1 and G2 (Fig. 1b), while increasing V_{G2} adds electrons to the neighboring electron QD (see corresponding labels). The hole QD exhibits a stronger readout contrast than the electron QD, consistent with its closer lateral proximity to the charge detector.

Note that V_{G1} influences the capacitive coupling between the charge detector and the QDs, and hence the detector sensitivity, via two mechanisms: (i) it shifts the lateral position of the QDs, changing their distance to the detector; (ii) it tunes the carrier density in the region between detector and QDs, thereby modifying the electrostatic screening. To study this in more detail, we extract the step height $\delta\phi_{\text{step}}$ as a function of V_{G1} for two distinct charge transitions (white and black dashed lines in Fig. 3a). For the (1h,xe) configuration—adding the first hole to the hole QD—we observe that the detector response increases as V_{G1} is made more negative (Fig. 3b). In contrast, for the (xh,2e) configuration—transitioning from one to two electrons in the electron QD—the response increases with more positive V_{G1} (Fig. 3c). To understand these opposing trends, we compare the experimental data with Schrödinger–Poisson simulations of the charge carrier density. The results show that the relative impact of (i) the QPC–QD distance and (ii) screening by intermediate charges depends on the spatial charge distribution. For the (1h,xe) case, the simulations reveal a change only in the amount of charge between the QD and the QPC charge detector (Fig. 3d), whereas in the (xh,2e) case the QPC position also shifts significantly (Fig. 3e). Consequently, the simulations reproduce the experimentally observed opposite trends in $\delta\phi_{\text{step}}$ as a function of V_{G1} (Figs. 3f,g). This agreement between experiment and simulation establishes a consistent picture of how V_{G1} controls the detector sensitivity via distance and screening effects.

In the following, we focus on the single-particle electron–hole regime. Fig. 4a shows a close-up of the (0h,0e) \leftrightarrow (1h,1e) charge transition (see Fig. 3a), corresponding to the creation and annihilation of electron–hole pairs [34]. Here, the different readout contrast for electrons and holes becomes more apparent. The inline arrangement of the QDs leads to strong contrast along the interdot transition ($\varepsilon = 0$) and reveals four clearly distinguishable charge states: (0h,0e), (1h,0e), (0h,1e), and (1h,1e). Fig. 4b shows a similar measurement as in Fig. 4a, but with an out-of-plane magnetic field of $B = 1.5 \text{ T}$ applied. The finite magnetic field reduces the interdot tunneling rates which is reflected in a random telegraph signal (RTS), close to the degeneracy of the (0h,0e) and (1h,1e) charge states, i.e. at $\varepsilon = 0$, indicating that time-resolved charge detection might be feasible.

To realize time-resolved charge detection, we optimized

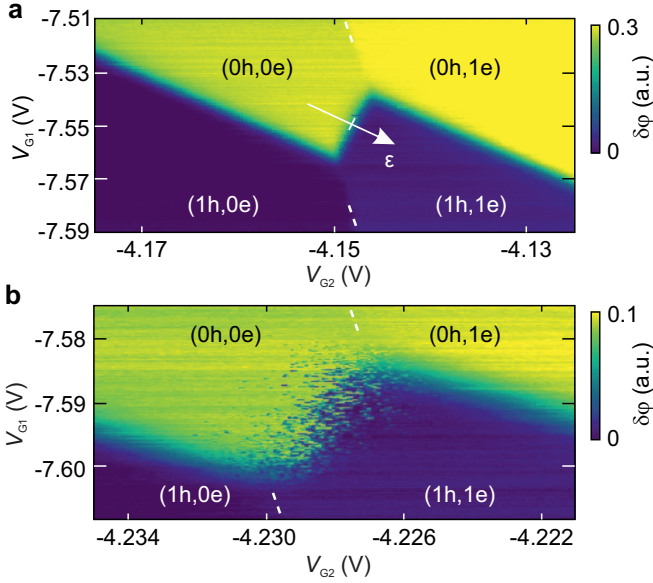


FIG. 4. (a) Charge stability diagram showing a close-up of the single-particle electron-hole transition measured in Fig. 3a at $B = 0$ T. ε is the detuning energy between the charge states $(0h,0e)$ and $(1h,1e)$. A linear background caused by capacitive cross talk between the gate voltages V_{G1} and V_{G2} and the charge detector was subtracted. (b) Same as in (a) but with a perpendicular magnetic field of $B = 1.5$ T applied.

the charge detector for high-bandwidth operation: electrostatic tuning (see discussion above) combined with RF carrier frequency and amplitude optimization increased the sensitivity and enabled bandwidths in the MHz range — an essential requirement for time-resolved QD state readout in qubit operation [9, 12–14, 43, 44]. We assess the performance of the charge detector for frequencies below the RF carrier frequency of around 115 MHz by measuring the time-dependent detector signal. Therefore, we reduce the tunneling rates by applying an out-of-plane magnetic field of $B = 1.3$ T, similar to Fig. 4b. Here, statistical tunnel events can be observed close to the degeneracy of the $(0h,0e)$ and $(1h,1e)$ charge states at $\varepsilon = 0$, hinting towards a low interdot tunneling rate. To investigate these processes in detail, we measure the demodulated phase $\delta\varphi$ of the reflected signal as a function of time using a digitizer card AlazarTech ATS9440. Exemplary, Fig. 5a shows 1 s long traces out of measurements, which took 50 s each. The three traces are measured at different V_{G1} . Individual tunneling events can be observed as an RTS between two levels corresponding to the $(0h,0e)$ (lower) and the $(1h,1e)$ (upper) charge configuration. The histograms on the right show the distribution of data points recorded over a time span of 50 s representing the occupation probability of the two charge configurations. At $\varepsilon = 0$ (red point in Fig. 5a,b), the DQD is found with equal probability in either of the two configurations. For finite detuning ($|\varepsilon| > 0$), the system is either predominantly in the $(1h,1e)$ configuration (orange point) or in the $(0h,0e)$ configuration (black point).

The corresponding color-coded positions in the charge stability diagram are shown in Fig. 5b. We apply a numerical equivalent of a *Schmitt trigger* [45] thresholding algorithm to detect single tunneling events and determine the times spans $\tau_{(1h,1e)}$ and $\tau_{(0,0)}$ during which the DQD is in the respective state. The rates of the charge transitions $(1h,1e) \rightarrow (0h,0e)$, are $\Gamma_{(1h,1e)} = 1/\langle\tau_{(1h,1e)}\rangle$ and $(0h,0e) \rightarrow (1h,1e)$, $\Gamma_{(0,0)} = 1/\langle\tau_{(0,0)}\rangle$, respectively [38, 46]. Fig. 5b shows the resulting rates $\Gamma_{(1h,1e)}$ (left) and $\Gamma_{(0,0)}$ (right) as a function of V_{G1} and V_{G2} at $B = 1.3$ T. At $\varepsilon < 0$, $\Gamma_{(1h,1e)}$ is increasing while $\Gamma_{(0,0)}$ is decreasing and vice versa for $\varepsilon > 0$. This result matches the RTS measurements in Figs. 5a. At $\varepsilon = 0$, we find equal transition rates of $\Gamma_{(1h,1e)} = \Gamma_{(0,0)} \approx 20$ Hz. Here, resonant tunneling between the electron and hole QD as well as co-tunneling from the reservoirs could contribute to the transition between the charge states [47]. We decrease the magnetic field to $B = 0.9$ T to increase the interdot coupling. Fig. 5c shows 20 ms long time traces that are taken from a measurement recorded for 5 s at different positions along the interdot transition (compare with Fig. 5a,b). Here, the tunneling events appear on timescales which are around 100 times faster than at $B = 1.3$ T (see Fig. 5a). To capture these events, the low pass cut-off frequency and the sampling rate of the Alazar card had to be increased to 77 kHz and 200 kS/s, respectively, leading to a decrease of the SNR. To quantify the effect of magnetic field tunable tunneling rates we measure the transition rates between the charge states $(0h,0e)$ and $(1h,1e)$ at $\varepsilon = 0$ as a function of B . The result is depicted in Fig. 5d and shows a strong dependency, following a power law of approximately $\Gamma \propto B^{-(10.0 \pm 0.7)}$. By fitting a double Gaussian function to the histograms, which are exemplary shown in Figs. 5a and b, the SNR can be extracted from the time-dependent measurements [48]. The corresponding data as a function of detection bandwidth is depicted in Fig. 5e (here, exemplary for $B = 0.7$ T). We find that a SNR above 2.5 is maintained for a bandwidth exceeding 250 kHz.

In summary, we demonstrate RF reflectometry charge detection of an electron-hole DQD in BLG using a capacitively coupled QPC. In average signal measurements of the charge detector response, we reach bandwidths up to 7 MHz and an SNR of up to 160. Improving the matching condition between the resonant circuit and the QPC can further increase the sensitivity of the charge detector. The sensitivity can be tuned electrostatically by using the finger gate in between the detector and QDs. We identify screening effects and the distance of the detector and QDs as the relevant mechanisms limiting the sensitivity by comparison with a model based on a self-consistent Schrödinger-Poisson solver. Finally, we demonstrate the distinction of the charge states of a single-particle electron-hole DQD in the time domain with a measurement bandwidth of up to 250 kHz, exceeding state-of-the-art experiments on electron QDs in BLG by a factor of 10 [38, 39]. With this technique, we

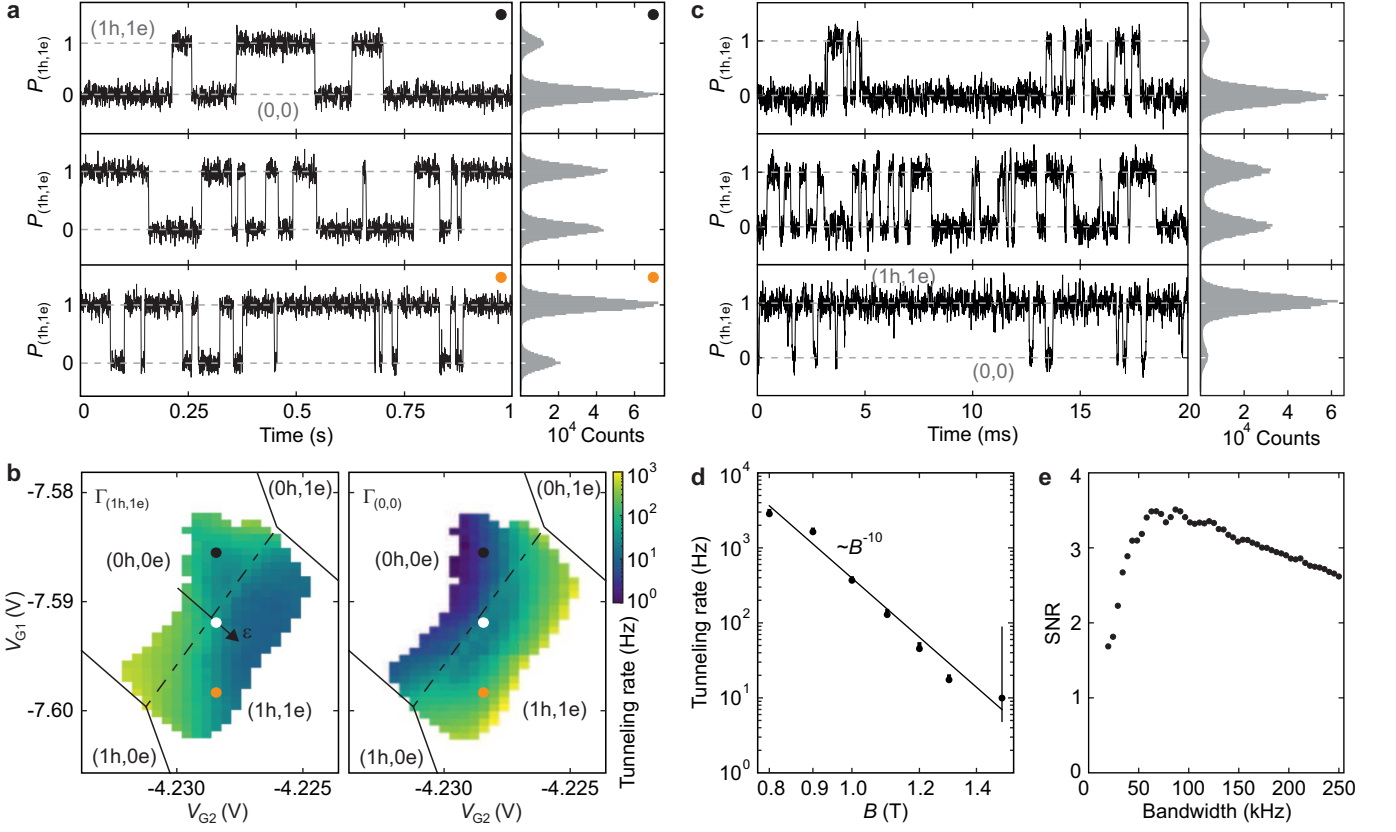


FIG. 5. (a) Time-resolved detection of $(0h,0e) \leftrightarrow (1h,1e)$ charge transitions at $B = 1.3$ T recorded in a time span of 1 s with a sampling rate of 20 kS/s. The data has been low pass filtered at 7.5 kHz. Histograms of the data sets with a trace length of 50 s are shown at the side. (b) Tunneling rates $\Gamma_{(1h,1e)}$ (left) and $\Gamma_{(0,0)}$ (right) for the annihilation and creation of an electron hole pair, respectively, as a function of V_{G1} and V_{G2} ($B = 1.3$ T). Each data point has been obtained from a single-shot measurement, as in (a). (c) Time-resolved detection in a regime of increased tunnel coupling at $B = 0.9$ T in a time span of 20 ms with a sampling rate of 200 kS/s. The data has been low pass filtered at 77 kHz. Histograms of the data sets with a trace length of 5 s are shown at the side. (d) Combined tunneling rate as a function of the perpendicular magnetic field B , determined at $\varepsilon = 0$. Fitting a power law yields $\Gamma \propto B^{-10.0 \pm 0.7}$. (e) SNR determined from time-resolved charge detection as a function of the measurement bandwidth ($B = 0.7$ T).

determine magnetic field dependent single electron-hole tunneling rates. Importantly, the electron-hole DQD in BLG is a particle-hole symmetric system with a robust single-particle spin and valley blockade [34]. This mechanism, together with the presented time domain measurements, may allow for high fidelity spin-to-charge and valley-to-charge conversion, providing a reliable read-out scheme for spin and valley states [20]. This paves the way for measurements of the relaxation and coherence times of spin and valley states, marking a milestone towards the realization of spin, valley and spin-valley qubits. Beside qubits, further applications of time-resolved readout of electron-hole DQDs in BLG may include wide band single-photon THz detectors [41, 49], electron-hole pair pumps [50] and Cooper pair splitters [51].

Acknowledgements The authors thank F. Lentz, S. Trellenkamp and M. Otto for help with sample fabrication. This project has received funding from the European Research Council (ERC) under grant agreement No. 820254, the Deutsche Forschungsgemeinschaft

(DFG, German Research Foundation) under Germany's Excellence Strategy - Cluster of Excellence Matter and Light for Quantum Computing (ML4Q) EXC 2004/1 - 390534769, through DFG (STA 1146/11-1), and by the Helmholtz Nano Facility [52]. K.W. and T.T. acknowledge support from the JSPS KAKENHI (Grant Numbers 21H05233 and 23H02052), the CREST (JPMJCR24A5), JST and World Premier International Research Center Initiative (WPI), MEXT, Japan. S.D. and F.L. gratefully acknowledge support by the Austrian Science Fund (FWF), doctoral college TU-DX (DOC 142-N, grant DOI 10.55776/DOC142). Electrostatics simulations were performed on the Vienna Scientific Cluster (VSC) 5.

Author contributions K.H., S.M. C.V. and C.S. conceived this experiment. K.H., S.M., H.D., S.R., and T.D. fabricated the device. K.H., S.M. and H.D. performed the measurements and analyzed the data with the help of L.V. and L.S.. S.D. and F.L. performed

the electrostatic simulations of the device architecture. K.W. and T.T. synthesized the hBN crystals. C.V. and C.S. supervised the project. K.H., S.M., H.D., C.V., Ş.D., F.L. and C.S. wrote the manuscript with contributions from all authors. K.H. and S.M. contributed

equally to this work.

Competing interests The authors declare no competing interests.

-
- [1] G. Burkard, T. D. Ladd, A. Pan, J. M. Nichol, and J. R. Petta, *Rev. Mod. Phys.* **95**, 025003 (2023).
 - [2] A. Chatterjee, P. Stevenson, S. De Franceschi, A. Morello, N. P. de Leon, and F. Kuemmeth, *Nat. Rev. Phys.* **3**, 157 (2021).
 - [3] F. Vigneau, F. Fedele, A. Chatterjee, D. Reilly, F. Kuemmeth, M. F. Gonzalez-Zalba, E. Laird, and N. Ares, *Appl. Phys. Rev.* **10** (2023), 10.1063/5.0088229.
 - [4] J. M. Elzerman, R. Hanson, J. S. Greidanus, L. H. Willems van Beveren, S. De Franceschi, L. M. K. Vandersypen, S. Tarucha, and L. P. Kouwenhoven, *Phys. Rev. B* **67**, 161308 (2003).
 - [5] T. Ihn, S. Gustavsson, U. Gasser, B. Küng, T. Müller, R. Schleser, M. Sigrist, I. Shorubalko, R. Leturcq, and K. Ensslin, *Solid State Commun.* **149**, 1419 (2009).
 - [6] R. J. Schoelkopf, P. Wahlgren, A. A. Kozhevnikov, P. Delsing, and D. E. Prober, *Science* **280**, 1238 (1998).
 - [7] D. J. Reilly, C. M. Marcus, M. P. Hanson, and A. C. Gossard, *Appl. Phys. Lett.* **91**, 162101 (2007).
 - [8] M. C. Cassidy, A. S. Dzurak, R. G. Clark, K. D. Petersson, I. Farrer, D. A. Ritchie, and C. G. Smith, *Appl. Phys. Lett.* **91**, 222104 (2007).
 - [9] J. M. Elzerman, R. Hanson, L. H. Willems van Beveren, B. Witkamp, L. M. K. Vandersypen, and L. P. Kouwenhoven, *Nature* **430**, 431 (2004).
 - [10] C. Volk, A. Chatterjee, F. Ansaloni, C. M. Marcus, and F. Kuemmeth, *Nano Lett.* **19**, 5628 (2019).
 - [11] Y.-Y. Liu, S. G. J. Philips, L. A. Orona, N. Samkharadze, T. McJunkin, E. R. MacQuarrie, M. A. Eriksson, L. M. K. Vandersypen, and A. Yacoby, *Phys. Rev. Appl.* **16**, 014057 (2021).
 - [12] A. Noiri, K. Takeda, T. Nakajima, T. Kobayashi, A. Sammak, G. Scappucci, and S. Tarucha, *Nature* **601**, 338 (2022).
 - [13] S. G. J. Philips, M. T. Madzik, S. V. Amitonov, S. L. de Snoo, M. Russ, N. Kalhor, C. Volk, W. I. L. Lawrie, D. Brousse, L. Trypouten, B. P. Wuetz, A. Sammak, M. Veldhorst, G. Scappucci, and L. M. K. Vandersypen, *Nature* **609**, 919 (2022).
 - [14] A. R. Mills, C. R. Guinn, M. J. Gullans, A. J. Sigillito, M. M. Feldman, E. Nielsen, and J. R. Petta, *Sci. Adv.* **8** (2022), 10.1126/sciadv.abn5130.
 - [15] M. T. Madzik, S. Asaad, A. Youssry, B. Joecker, K. M. Rudinger, E. Nielsen, K. C. Young, T. J. Proctor, A. D. Baczewski, A. Laucht, V. Schmitt, F. E. Hudson, K. M. Itoh, A. M. Jakob, B. C. Johnson, D. N. Jamieson, A. S. Dzurak, C. Ferrie, R. Blume-Kohout, and A. Morello, *Nature* **601**, 348 (2022).
 - [16] W. I. L. Lawrie, M. Rimbach-Russ, F. v. Riggelen, N. W. Hendrickx, S. L. d. Snoo, A. Sammak, G. Scappucci, J. Helsen, and M. Veldhorst, *Nat. Commun.* **14**, 3617 (2023).
 - [17] C. L. Kane and E. J. Mele, *Phys. Rev. Lett.* **95**, 226801 (2005).
 - [18] S. Konschuh, M. Gmitra, D. Kochan, and J. Fabian, *Phys. Rev. B* **85**, 115423 (2012).
 - [19] M. Wojtaszek, I. J. Vera-Marun, E. Whiteway, M. Hilke, and B. J. van Wees, *Phys. Rev. B* **89**, 035417 (2014).
 - [20] B. Trauzettel, D. V. Bulaev, D. Loss, and G. Burkard, *Nat. Phys.* **3**, 192 (2007).
 - [21] E. Icking, L. Banszerus, F. Wörtche, F. Volmer, P. Schmidt, C. Steiner, S. Engels, J. Hesselmann, M. Goldsche, K. Watanabe, T. Taniguchi, C. Volk, B. Beschoten, and C. Stampfer, *Adv. Electron. Mater.* **8**, 2200510 (2022).
 - [22] H. Overweg, H. Eggimann, X. Chen, S. Slizovskiy, M. Eich, R. Pisoni, Y. Lee, P. Rickhaus, K. Watanabe, T. Taniguchi, V. Fal'ko, T. Ihn, and K. Ensslin, *Nano Lett.* **18**, 553 (2018).
 - [23] L. Banszerus, B. Frohn, T. Fabian, S. Somanchi, A. Epping, M. Müller, D. Neumaier, K. Watanabe, T. Taniguchi, F. Libisch, B. Beschoten, F. Hassler, and C. Stampfer, *Phys. Rev. Lett.* **124**, 177701 (2020).
 - [24] M. Eich, F. Herman, R. Pisoni, H. Overweg, A. Kurzmam, Y. Lee, P. Rickhaus, K. Watanabe, T. Taniguchi, M. Sigrist, T. Ihn, and K. Ensslin, *Phys. Rev. X* **8**, 031023 (2018).
 - [25] L. Banszerus, A. Rothstein, T. Fabian, S. Möller, E. Icking, S. Trellenkamp, F. Lentz, D. Neumaier, K. Watanabe, T. Taniguchi, F. Libisch, C. Volk, and C. Stampfer, *Nano Lett.* **20**, 7709 (2020).
 - [26] L. Banszerus, S. Möller, C. Steiner, E. Icking, S. Trellenkamp, F. Lentz, K. Watanabe, T. Taniguchi, C. Volk, and C. Stampfer, *Nat. Commun.* **12**, 5250 (2021).
 - [27] A. Kurzmam, M. Eich, H. Overweg, M. Mangold, F. Herman, P. Rickhaus, R. Pisoni, Y. Lee, R. Garreis, C. Tong, K. Watanabe, T. Taniguchi, K. Ensslin, and T. Ihn, *Phys. Rev. Lett.* **123**, 026803 (2019).
 - [28] S. Möller, L. Banszerus, A. Knothe, C. Steiner, E. Icking, S. Trellenkamp, F. Lentz, K. Watanabe, T. Taniguchi, L. I. Glazman, V. I. Fal'ko, C. Volk, and C. Stampfer, *Phys. Rev. Lett.* **127**, 256802 (2021).
 - [29] L. Banszerus, K. Hecker, S. Möller, E. Icking, K. Watanabe, T. Taniguchi, C. Volk, and C. Stampfer, *Nat. Commun.* **13**, 3637 (2022).
 - [30] L. Banszerus, K. Hecker, L. Wang, S. Möller, K. Watanabe, T. Taniguchi, G. Burkard, C. Volk, and C. Stampfer, *Phys. Rev. B* **112**, 035409 (2025).
 - [31] C. Tong, R. Garreis, A. Knothe, M. Eich, A. Sacchi, K. Watanabe, T. Taniguchi, V. Fal'ko, T. Ihn, K. Ensslin, and A. Kurzmam, *Nano Lett.* **21**, 1068 (2021).
 - [32] C. Tong, A. Kurzmam, R. Garreis, K. Watanabe, T. Taniguchi, T. Ihn, and K. Ensslin, *Phys. Rev. Res.* **6**, L012006 (2024).
 - [33] S. Möller, L. Banszerus, K. Hecker, H. Dulisch, K. Watanabe, T. Taniguchi, C. Volk, and C. Stampfer, *Phys. Rev. B* **111**, 165416 (2025).
 - [34] L. Banszerus, S. Möller, K. Hecker, E. Icking, K. Watan-

- abe, T. Taniguchi, F. Hassler, C. Volk, and C. Stampfer, *Nature* **618**, 51 (2023).
- [35] A. Kurzmann, H. Overweg, M. Eich, A. Pally, P. Rickhaus, R. Pisoni, Y. Lee, K. Watanabe, T. Taniguchi, T. Ihn, and K. Ensslin, *Nano Lett.* **19**, 5216 (2019).
 - [36] L. Banszerus, S. Möller, E. Icking, C. Steiner, D. Neumaier, M. Otto, K. Watanabe, T. Taniguchi, C. Volk, and C. Stampfer, *Appl. Phys. Lett.* **118**, 093104 (2021).
 - [37] M. J. Ruckriegel, L. M. Gächter, D. Kealhofer, M. Bahrami Panah, C. Tong, C. Adam, M. Masseroni, H. Duprez, R. Garreis, K. Watanabe, T. Taniguchi, A. Wallraff, T. Ihn, K. Ensslin, and W. W. Huang, *Nano Lett.* **24**, 7508 (2024).
 - [38] R. Garreis, J. D. Gerber, V. Stará, C. Tong, C. Gold, M. Rösli, K. Watanabe, T. Taniguchi, K. Ensslin, T. Ihn, and A. Kurzmann, *Phys. Rev. Res.* **5**, 013042 (2023).
 - [39] L. M. Gächter, R. Garreis, J. D. Gerber, M. J. Ruckriegel, C. Tong, B. Kratochwil, F. K. de Vries, A. Kurzmann, K. Watanabe, T. Taniguchi, T. Ihn, K. Ensslin, and W. W. Huang, *PRX Quantum* **3**, 020343 (2022).
 - [40] R. Garreis, C. Tong, J. Terle, M. J. Ruckriegel, J. D. Gerber, L. M. Gächter, K. Watanabe, T. Taniguchi, T. Ihn, K. Ensslin, and W. W. Huang, *Nat. Phys.* **20**, 428 (2024).
 - [41] D. A. Bandurin, D. Svintsov, I. Gayduchenko, S. G. Xu, A. Principi, M. Moskotin, I. Tretyakov, D. Yagodkin, S. Zhukov, T. Taniguchi, K. Watanabe, I. V. Grigorieva, M. Polini, G. N. Goltsman, A. K. Geim, and G. Fedorov, *Nat. Commun.* **9**, 5392 (2018).
 - [42] J. Schöberl, “A high performance multiphysics finite element software,” <https://ngsolve.org/> (2024).
 - [43] N. O. Antoniadis, M. R. Hogg, W. F. Stehl, A. Javadi, N. Tömm, R. Schott, S. R. Valentin, A. D. Wieck, A. Ludwig, and R. J. Warburton, *Nat. Commun.* **14**, 3977 (2023).
 - [44] F. Hoehne, C. Huck, M. S. Brandt, and H. Huebl, *Phys. Rev. B* **89**, 161305 (2014).
 - [45] P. Horowitz and W. Hill, *The art of electronics; 3rd ed.* (Cambridge University Press, Cambridge, 2015) p. 237.
 - [46] J. Güttinger, J. Seif, C. Stampfer, A. Capelli, K. Ensslin, and T. Ihn, *Phys. Rev. B* **83**, 165445 (2011).
 - [47] W. G. van der Wiel, S. De Franceschi, J. M. Elzerman, T. Fujisawa, S. Tarucha, and L. P. Kouwenhoven, *Rev. Mod. Phys.* **75**, 1 (2002).
 - [48] S. Gustavsson, R. Leturcq, M. Studer, I. Shorubalko, T. Ihn, K. Ensslin, D. C. Driscoll, and A. C. Gossard, *Surf. Sci. Rep.* **64**, 191 (2009).
 - [49] E. Riccardi, S. Massabeau, F. Valmorra, S. Messelot, M. Rosticher, J. Tignon, K. Watanabe, T. Taniguchi, M. Delbecq, S. Dhillon, R. Ferreira, S. Balibar, T. Kontos, and J. Mangeney, *Nano Lett.* **20**, 5408 (2020).
 - [50] A. Bordoloi, V. Zannier, L. Sorba, C. Schönenberger, and A. Baumgartner, *Nature* **612**, 454 (2022).
 - [51] G. Wang, T. Dvir, G. P. Mazur, C.-X. Liu, N. van Loo, S. L. D. Ten Haaf, A. Bordin, S. Gazibegovic, G. Badawy, E. P. A. M. Bakkers, M. Wimmer, and L. P. Kouwenhoven, *Nature* **612**, 448 (2022).
 - [52] W. Albrecht, J. Moers, and B. Hermanns, *Journal of Large-Scale Research Facilities* **3**, 112 (2017).

Radio-frequency charge detection on graphene electron-hole double quantum dots – Supplementary Information –

K. Hecker,^{1,2,*} S. Möller,^{1,2,*} H. Dulisch,^{1,2} Ş. Duman,³ L. Stecher,¹ L. Valerius,¹ T. Deußen,¹
S. Ravuri,¹ K. Watanabe,⁴ T. Taniguchi,⁵ F. Libisch,³ C. Volk,^{1,2} and C. Stampfer^{1,2,†}

¹*JARA-FIT and 2nd Institute of Physics, RWTH Aachen University, 52074 Aachen, Germany, EU*

²*Peter Grünberg Institute (PGI-9), Forschungszentrum Jülich, 52425 Jülich, Germany, EU*

³*Institute for Theoretical Physics, TU Wien, 1040 Vienna, Austria, EU*

⁴*Research Center for Functional Materials, National Institute for Materials Science, 1-1 Namiki, Tsukuba 305-0044, Japan*

⁵*International Center for Materials Nanoarchitectonics,*

National Institute for Materials Science, 1-1 Namiki, Tsukuba 305-0044, Japan

(Dated: September 16, 2025)

A. Device design

The device consists of a van der Waals heterostructure of BLG encapsulated between two crystals of hexagonal boron nitride (hBN), each approximately 50 nm thick, placed on a graphitic back gate (BG). Ohmic Cr/Au contacts are etched through the top hBN flake to the BLG. Fig. 1a of the Manuscript shows a false color scanning electron microscope (SEM) image of the metallic gate structure fabricated on top of the heterostructure. Split gates (SGs) and a graphite BG are used to open a band gap in the BLG, and to form conducting channels. In the wide channel (highlighted in blue), a QPC beneath the finger gate G0 (orange) acts as a capacitively coupled charge detector. This channel forms a T-junction with the narrow channel beneath the other finger gates (FGs), where the QDs will be localized. A layer of 15 nm Al₂O₃ is placed on top of the SGs, separating them from the Cr/Au FGs (orange outlines), which define and control the QDs and the QPC. These FGs have a center-to-center pitch of 140 nm and a width of 70 nm. The center of the wide channel has a lateral distance of 230 nm to the center of FG G2. To control the tunnel barriers between the QDs, the QPC charge detector and the reservoirs, an additional layer of FGs (green outlines) is placed on top, separated by another 15 nm Al₂O₃ [1]. For more details on the fabrication of the device, we refer to Ref. [2].

B. Schrödinger-Poisson model

The local charge carrier density $\rho[\phi(\mathbf{r}'), \partial_z \phi(\mathbf{r}')](\mathbf{r})$ can be simulated by solving Poisson's equation in dielectric media

$$\nabla(\varepsilon(\mathbf{r})\nabla\phi(\mathbf{r})) = \rho[\phi(\mathbf{r}'), \partial_z \phi(\mathbf{r}')](\mathbf{r}), \quad (1)$$

where $\varepsilon(\mathbf{r})$ represents the local dielectric constants of the materials, and $\phi(\mathbf{r})$ the electrostatic potential. If all permittivities were the same, i.e. $\varepsilon(\mathbf{r}) = \text{const.}$, the gradient

applied to it would be zero and we would get a single Laplacian on the left-hand side. However, the device consists of materials with different permittivities, hence $\varepsilon(\mathbf{r})$ changes at interfaces. We account for this by the more general expression above, which can also accommodate tensor-valued ε necessary for different in-plane and out-of-plane permittivities. The voltages at the different gates serve as Dirichlet boundary conditions for $\phi(\mathbf{r})$; at all other boundary points we assume Neumann boundary conditions, $\frac{\partial \phi}{\partial \vec{n}} = 0$, where \vec{n} is the normal vector to the surface of the structure at a given boundary point \vec{r}_b . We assume only BLG carries a charge carrier density, which depends on the local displacement field and its gradient. Consequently, $\rho[\phi(\mathbf{r}'), \partial_z \phi(\mathbf{r}')](\mathbf{r})$ depends on $\phi(\mathbf{r}')$ for the local shift in potential, and $\partial_z \phi(\mathbf{r}')$ for the local band gap. We use a local density approximation,

$$\rho[\phi, \partial_z \phi](\mathbf{r}) \approx \rho(\phi(\mathbf{r}), \partial_z \phi(\mathbf{r})) \approx - \int_0^{\phi(\mathbf{r})} D(\varepsilon'; \partial_z \phi(\mathbf{r})) d\varepsilon' \quad (2)$$

with $D(\varepsilon'; \partial_z \phi(\mathbf{r}))$ being the density of states per unit area of BLG divided by its thickness (to obtain a volume density) at a given energy and displacement field $\partial_z \phi(\mathbf{r})$. To simplify further, we assume that the charge carrier density $\rho(x, y, z) = \rho(x, y)$ may only vary in-plane, but not out-of-plane within the 3.35 Å thickness of BLG. This allows replacing the upper integration bound in Eq. (2) $\phi(\mathbf{r})$, which varies as a function of three coordinates, by the mean evaluated at the top and bottom height of the BLG sheet at given in-plane coordinates,

$$\phi(\mathbf{r}) \rightarrow \bar{\phi}(x, y) = 0.5 \cdot (\phi(x, y, z_{\text{bot.}}) + \phi(x, y, z_{\text{top}}))$$

With a self-consistency loop, the charge carrier density in BLG can be numerically calculated for a given set of gate voltages. We start with an initial guess by solving the homogeneous problem, i.e. we set the right-hand side of Eq. (1) to zero and obtain ϕ_0 . This first result ϕ_0 strongly overestimates the induced charge, since no screening is considered. To better condition the start of the self-consistency cycle, we therefore multiply ϕ_0 by a small number $\gamma \approx 0.025 \ll 1$ while leaving the gradient unchanged. Thus, we evaluate the first induced ρ_1 by

* These two authors contributed equally.

† stampfer@physik.rwth-aachen.de

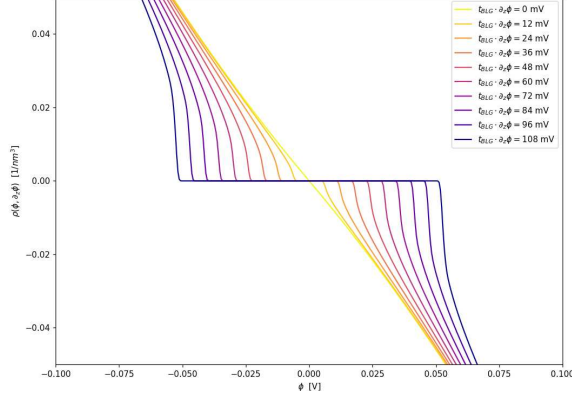


FIG. S1. Charge carrier density (Eq. (2)) as a function of potential ϕ for different gradients $\partial_z\phi$. The plateau at $\rho = 0$ emerges due to the opening band gap. Note the resulting strong nonlinearity at the band edge. We assume electron-hole symmetry.

inserting into Eq. (2)

$$\rho_1 = \rho[\gamma \cdot \phi_0, 1 \cdot \partial_z \phi_0]$$

This rescaling of ϕ_0 but not $\partial_z \phi_0$ is only done for the very first iteration to obtain an initial guess for ρ_1 . For all subsequent iterations we try to find the root of the function

$$\rho_n - \rho[\phi_n, \partial_z \phi_n] = 0 \quad (3)$$

where ϕ_n is the solution of Eq. (1) with the right-hand side ρ_n , which we calculate with NGSolve [3]. At each iteration, the root finder provides a ρ_n for which we solve Poisson's Eq. (1), yielding ϕ_n . The latter we insert into Eq. (2) for the charge carrier density, and compare $\rho[\phi_n, \partial_z \phi_n]$ to ρ_n . We iterate this procedure until both values (approximately) agree and thus self-consistency is achieved. The difference between the inhomogeneity and the model in Eq. (3) is computed on a rectangular grid of $N = 200 \cdot 200 = 40 \cdot 10^3$ points inside the BLG crystal. Solving the non-linear Poisson's equation 1 amounts to finding a root of a vector-valued function with dimension of $N = 40 \cdot 10^3$.

The main challenge of the self-consistency Eq. (2) is the band gap in the density of states, the integrand of Eq. (2), which changes locally as a function of the out-of-plane derivative $\partial_z \phi(\mathbf{r})$. As depicted in Fig. S1, charge carriers are absent in the band gap. Two kinks show up in the charge carrier density at the Van Hove singularities due to the band edges. As a consequence, the right-hand side of Eq. (2) cannot be linearized locally at every point, thus the tested gradient methods, such as the "good" and "bad" Broyden methods to obtain the root of function 3, fail. However, we find that the derivative free spectral residual method [4] does work in finding the root of

Eq. (3). We use the *scipy.optimize.root* implementation [5].

The average potential difference $\delta\phi$ at the QPC caused by a change in occupation depicted in the simulation curve in the main text (Fig. 3(f)) can be made more precise:

$$\delta\phi = \langle \phi \{V_{(i)}\} \rangle_{\text{QPC}} - \langle \phi \{V_{(i)} + \delta V_{(i)}\} \rangle_{\text{QPC}}$$

For this expression, we first calculate the electric potential ϕ at a specific configuration (for instance in Fig. 3(e) of the main text we go along a section of the $(1e, 0h)$ to $(2e, 0h)$ charge transition line in the charge stability diagram) but for different voltages $\{V_{(i)}\}$. Once this line $\{V_{(i)}\}$ is found, we perform another simulation for a small deviation $\delta V_{(i)}$ along this section in the charge-stability diagram. Experimentally, the QPC (and in consequence the measured step height) is sensitive to this change of the electric potential

$$\phi_{\text{diff}} = \phi\{V_{(i)}\} - \phi\{V_{(i)} + \delta V_{(i)}\}$$

We map this function to a single scalar value by calculating the averages of the individual potentials inside BLG under the QPC ($\langle \dots \rangle_{\text{QPC}}$). This measure allows us to make general qualitative statements about the change of the magnitude of ϕ_{diff} . However, for a quantitative prediction one also needs to model the bound state spectrum of the BLG Hamiltonian and additionally account for screening due to the integer occupation of electrons and holes. This improvement of the model is computationally very challenging and left for future publications. Nevertheless, since the QPC is far away from the charges, we expect the qualitative trends of Fig. 3 (main text) to hold even in this case. We only expect corrections in the amplitude of ϕ_{diff} and in the immediate vicinity of the electron and hole bound states, leaving the functional form of the long-range electrostatic field intact.

material	ϵ
vacuum	1
polycarbonate	3.1
Al ₂ O ₃	9.1
hBN	4.98
hBN _⊥	3.03
BLG	1.8
BLG _⊥	3

TABLE I. Scalar and tensor permittivities ϵ of the materials relevant in the experiment. For hBN and BLG we distinguish between in-plane $\epsilon_{||}$ and out-of-plane ϵ_{\perp} permittivities (see [6] and [7]).

Fig. S2 shows a simulation of the potential ϕ_0 solving the homogeneous problem for the investigated device geometry and an exemplary set of gate voltages. Poisson's equation requires permittivities for each material. We use the scalar relative permittivities ϵ as given in Tab. I.

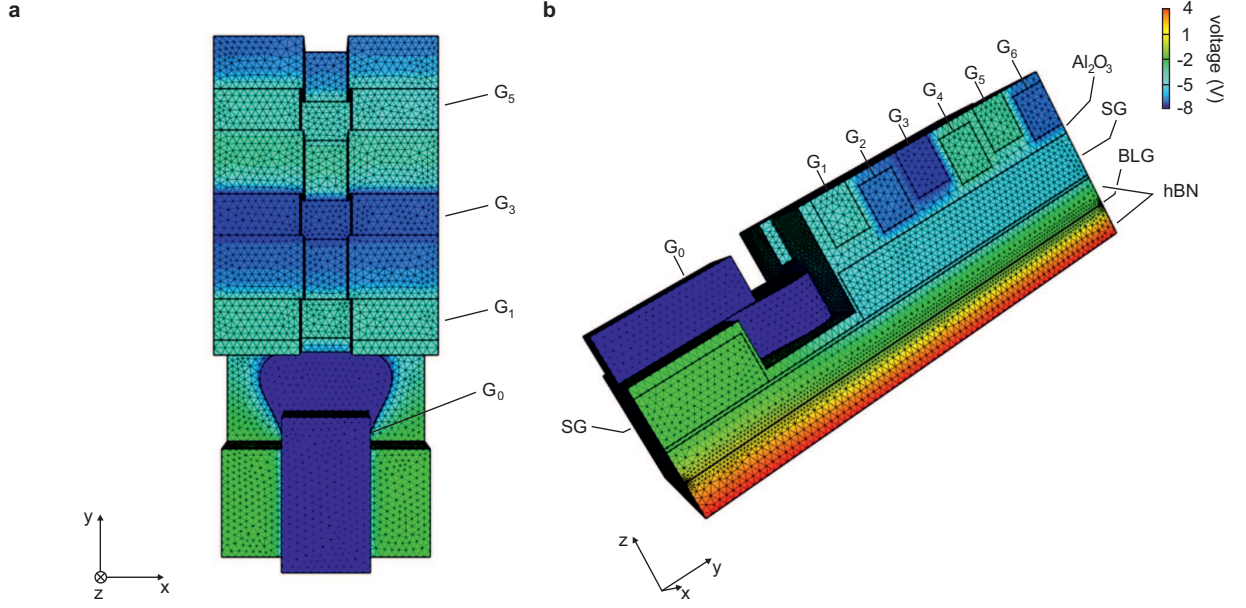


FIG. S2. (a) Top view and (b) side view of a 3D model of the used device, showing the heterostructure and the gate stack. The color code shows the voltages applied to the gates and the calculated potential throughout the device. A layer of vacuum covering the top gates filling out the simulation box is not shown for visibility.

-
- [1] L. Banszerus, A. Rothstein, E. Icking, S. Möller, K. Watanabe, T. Taniguchi, C. Stampfer, and C. Volk, Tunable interdot coupling in few-electron bilayer graphene double quantum dots, *Appl. Phys. Lett.* **118**, 103101 (2021).
 - [2] L. Banszerus, A. Rothstein, T. Fabian, S. Möller, E. Icking, S. Trellenkamp, F. Lentz, D. Neumaier, K. Watanabe, T. Taniguchi, F. Libisch, C. Volk, and C. Stampfer, Electron-Hole Crossover in Gate-Controlled Bilayer Graphene Quantum Dots, *Nano Lett.* **20**, 7709 (2020).
 - [3] J. Schöberl, A high performance multiphysics finite element software, <https://ngsolve.org/> (2024).
 - [4] W. La Cruz, J. M. Martínez, and M. Raydan, Spectral residual method without gradient information for solving large-scale nonlinear systems of equations, *Mathematics of Computation* **75**, 1429 (2006).
 - [5] P. Virtanen, R. Gommers, T. E. Oliphant, M. Haberland, T. Reddy, D. Cournapeau, E. Burovski, P. Peterson, W. Weckesser, J. Bright, S. J. van der Walt, M. Brett, J. Wilson, K. J. Millman, N. Mayorov, A. R. J. Nelson, E. Jones, R. Kern, E. Larson, C. J. Carey, Í. Polat, Y. Feng, E. W. Moore, J. VanderPlas, D. Laxalde, J. Perktold, R. Cimrman, I. Henriksen, E. A. Quintero, C. R. Harris, A. M. Archibald, A. H. Ribeiro, F. Pedregosa, P. van Mulbregt, and SciPy 1.0 Contributors, *SciPy 1.0: Fundamental Algorithms for Scientific Computing in Python*, *Nature Methods* **17**, 261 (2020).
 - [6] A. Laturia, M. L. Van de Put, Vandenberghe, and W. G., Dielectric properties of hexagonal boron nitride and transition metal dichalcogenides: from monolayer to bulk, *npj 2D Materials and Applications* volume **4** (2020).
 - [7] E. J. G. Santos and E. Kaxiras, Electric-field dependence of the effective dielectric constant in graphene, *Nano Letters* **13**, 898 (2013), pMID: 23339637.